Mapping spin–charge conversion to the band structure in a topological oxide two-dimensional electron gas

Diogo Vaz, Paul Noël, Annika Johansson, Börge Göbel, Flavio Bruno, Gyanendra Singh, Siobhan Mckeown-Walker, Felix Trier, Luis Vicente-Arche, Anke Sander, et al.

Mapping spin-charge conversion to the band structure in a topological oxide two-dimensional electron gas

Diogo C. Vaz[1]*, Paul Noël[2]*, Annika Johansson[3,4]*, Börge Göbel[3]*, Flavio Bruno[5], Gyanendra Singh[6], Siobhan McKeown-Walker[5], Felix Trier[1], Luis M. Vicente-Arche[1], Anke Sander[1], Sergio Valencia[7], Pierre Bruneel[8], Manali Vivek[8], Marc Gabay[8], Nicolas Bergeal[6], Felix Baumberger[5], Hanako Okuno[9], Agnès Barthélémy[1], Albert Fert[1], Laurent Vila[2♥], Ingrid Mertig[4,3], Jean-Philippe Attané[2] and Manuel Bibes[1♦]

[1] Unité Mixte de Physique CNRS, Thales, Univ. Paris-Sud, Université Paris-Saclay, 91767 Palaiseau (France)

[2] Univ. Grenoble Alpes, CEA, CNRS, Grenoble INP, INAC-Spintec, 38000 Grenoble (France)

[3] Max Planck Institute of Microstructure Physics, 06120 Halle (Germany)

[4] Institute of Physics, Martin Luther University Halle-Wittenberg, 06099 Halle (Germany)

[5] Department of Quantum Matter Physics, University of Geneva, 24 Quai Ernest Ansermet, 1211 Geneva (Switzerland)

[6] Laboratoire de Physique et d'Etude des Matériaux, ESPCI Paris, PSL Research University, CNRS, 10 Rue Vauquelin, 75005, Paris (France)

[7] Helmholtz-Zentrum Berlin für Materialien und Energie, Albert-Einstein-Strasse 15, 12489 Berlin (Germany)

[8] Laboratoire de Physique des Solides, CNRS, Univ. Paris-Sud, Université Paris-Saclay, 91405 Orsay (France)

[9] Univ. Grenoble Alpes, CEA, INAC-MEM, 38000 Grenoble (France)

While classical spintronics has traditionally relied on ferromagnetic metals as spin generators and spin detectors, a new approach called spin-orbitronics exploits the interplay between charge and spin currents enabled by the spin-orbit coupling (SOC) in non-magnetic systems. Efficient spin-charge interconversion can be realized through the direct and inverse Edelstein effects at interfaces where broken inversion symmetry induces a Rashba SOC. Although the simple Rashba picture of split parabolic bands is usually used to interpret such experiments, it fails to explain the largest conversion effects and their relation to the actual electronic structure. Here, we demonstrate a very large spin-to-charge conversion effect (inverse Edelstein length λ_{IEE} > 20 nm) in an interface-engineered high-carrier-density $SrTiO_3$ two-dimensional electron gas (2DEG) and use angle-resolved photoemission measurements and Boltzmann calculations to map its peculiar gate dependence to the band structure. We show that the conversion process is amplified by enhanced Rashba-like splitting due to orbital mixing, and in the vicinity of avoided band crossings with topologically non-trivial order. Our results indicate that oxide 2DEGs formed by a simple room-temperature sputtering procedure are strong candidates for spin-based information readout in novel memory and transistor designs. At the same time, they confirm the promise of topology as a new ingredient to expand the scope of complex oxides for spintronics.

* these authors contributed equally to this work. ♥ laurent.vila@cea.fr ♦ manuel.bibes@cnrs-thales.fr

The Rashba effect is a quantum phenomenon that occurs at surfaces and interfaces where spatial symmetry breaking results in an out-of-plane electric field[1]. In the presence of spin-orbit coupling (SOC), this leads to a lifting of the spin degeneracy and a locking of the momentum and spin degrees of freedom causing pairs of Fermi contours with a momentum splitting and opposite spin chiralities[2]. When a two-dimensional (2D) charge current j_c^{2D} flows in a Rashba system, it generates a transverse spin density through the Edelstein effect (EE) (also called Rashba-Edelstein or inverse spin galvanic effect)[3]. This spin density can diffuse in an adjacent conducting material through the interface, generating a three-dimensional (3D) pure spin current j_s^{3D} without net charge current (that is, a pure flow of spin angular momentum, with opposite flows for electrons of opposite spins). Conversely, the injection of a spin current into a Rashba system generates a net charge current (inverse Edelstein effect, IEE or spin galvanic effect)[4]. The EE and IEE can also be realized at surfaces of three-dimensional topological insulators[5], and have been predicted in other types of quantum materials[6,7].

The interpretation of the IEE in topological insulators is relatively simple since they usually have only one Fermi contour. The figure of merit $\lambda_{IEE} = j_c^{2D}/j_s^{3D}$ is given by the product of the Fermi velocity v_f and the momentum relaxation time τ (Ref. [8]). However, the situation is more complex in Rashba systems, where conversion occurs in two inequivalent Fermi contours whose contributions partially compensate each other[4,9], so that $\lambda_{IEE} = \alpha_R \tau/\hbar$ (in the approximation of circular Fermi contours) with α_R the Rashba coefficient. Unexpectedly, the largest λ_{IEE} values (6.4 nm) were not reported for topological insulators but for $SrTiO_3$-based two-dimensional electron gases (2DEGs) with a moderate effective Rashba SOC[10]. This unconventional result has been ascribed to the long relaxation time and to the multi-orbital nature of the system[10,11]. However, a detailed understanding is still lacking.

A 2DEG at the interface between $SrTiO_3$ (STO) and another perovskite insulator, $LaAlO_3$ (LAO), first discovered by Ohtomo and Hwang in 2004[12], possesses many interesting attributes including low-temperature superconductivity and a carrier density that is highly tunable by a gate voltage[13]. While the mechanisms for 2DEG formation remain debated, it is universally found that a thickness of at least four unit cells of LAO is needed for the 2DEG to appear[14] (although it can be reduced by metal capping[15,16]). Beyond this threshold, the properties of the 2DEG vary little with LAO thickness. Very recently, Rödel et al. reported that a 2DEG could also be formed in STO through the deposition of a few Å of Al at room temperature[17]. This approach has several advantages as it alleviates the need for the high temperature growth of crystalline LAO and allows the modulation of the carrier density over a broader range, through the adjustment of the Al thickness or the use of other metals[18]. Here, we report a very large inverse Edelstein effect in such Al/STO 2DEGs. The conversion efficiency and its sign strongly depend on the gate voltage, with λ_{IEE} reaching values in the range of ±20 nm. We quantitatively relate these values to the Fermi-energy-dependent Edelstein effect calculated within

the semi-classical Boltzmann transport theory applied to the experimentally determined electronic structure.

Following Ref. [17] we prepared STO 2DEGs by depositing an ultra-thin layer of Al (nominal thickness 9 Å) on TiO_2-terminated STO substrates using magnetron sputtering (see Methods). For scanning transmission electron microscopy (STEM), magnetotransport and spin-pumping experiments, we grew an additional NiFe layer and an AlO_x cap (3 nm in thickness) in the same vacuum cycle. The NiFe thickness was 2.5 nm for transport and 20 nm for STEM and spin-pumping. To evaluate the interaction between Al and the first few layers of STO, we performed in situ X-ray photoelectron spectroscopy (XPS) experiments focusing on the Ti 2p and Al 2p states (Fig. 1a). The spectrum collected for a bare STO substrate (grey area) corresponds to a Ti^{4+} valence state, consistent with its insulating character. Upon deposition of the ultrathin Al layer, two peaks associated with Ti^{3+} and Ti^{2+} valence states arise, pointing to the reduction of the STO and the generation of an electron-rich layer at its interface with Al. The spectral weight of these peaks is larger than normally observed in LAO/STO heterostructures[16,19], indicating a higher electron density. In the inset, we see that the Al 2p signal comprises two spectral features, corresponding to oxidized and metallic Al (high and low binding energies, respectively) and suggesting that the Al is largely oxidized. As previously reported[17], we conclude that Al is able to react with the surface oxygens and thus induces oxygen vacancies acting as electron donors in the first few layers of STO. From here on we thus refer to these samples as AlO_x/STO.

We have also characterized the interface by cross sectional STEM analysis. As seen in the Z-contrast in high-angle annular dark field (HAADF) images of Figures 1d and 1e, a continuous Al-rich layer can be identified, between the TiO_2-terminated $SrTiO_3$ surface and the NiFe layer, with a uniform thickness over all observed areas in the STEM specimen. The AlO_x thickness estimated using HAADF Z contrast is 1.0±0.1 nm, consistent with the deposition of 0.9 nm of Al metal and its volume expansion upon oxidation. Sr, Ti, Al and O elemental chemical maps have been acquired using electron dispersive X-ray spectroscopy (EDX), and show that oxygen is present in STO but also extends through the Al layer. A tiny amount of Ti also appears to be present in the Al-rich region. Overall, the STEM analysis corroborates the XPS data and clearly evidences that the Al layer is oxidized at the STO interface.

To estimate the spatial distribution of the Ti^{3+}-rich layer, we performed angle-dependent XPS experiments (cf. Fig. 1b) and electron energy loss spectroscopy (EELS) at the Ti $L_{3,2}$ edge (cf. Fig. 1c). EELS data in the Al-rich region (see Supplementary Material) suggest that most of the Ti^{2+} seen in XPS is found within the Al-rich layer. In Fig. 1b, we plot the ratio between the weights of the Ti^{3+} and Ti^{4+}

peaks, that increases exponentially with the XPS electron take-off angle, indicating a larger concentration of Ti^{3+} closer to the interface. The data are well fitted using a depth-profile model, previously used to estimate the thickness of 2DEG in LAO/STO samples[19]. We extract a total electron density of 7.2±1.0×10^{14} cm^{-2} and a thickness of 1.4±0.4 nm, confirming the quasi 2D nature of the electron gas. The mixed valence of Ti in STO is also seen in the EELS data presented in Fig. 1c, that we simulated with linear combinations of Ti^{3+} and Ti^{4+} reference signals (taking into account the experimental resolution). The extracted Ti^{3+} content is plotted in Fig. 1f, and is found to decrease when going deeper into the STO. The total Ti^{3+} concentration corresponds to an electron density of 6.3±1.0×10^{14} cm^{-2}, consistent with the XPS analysis.

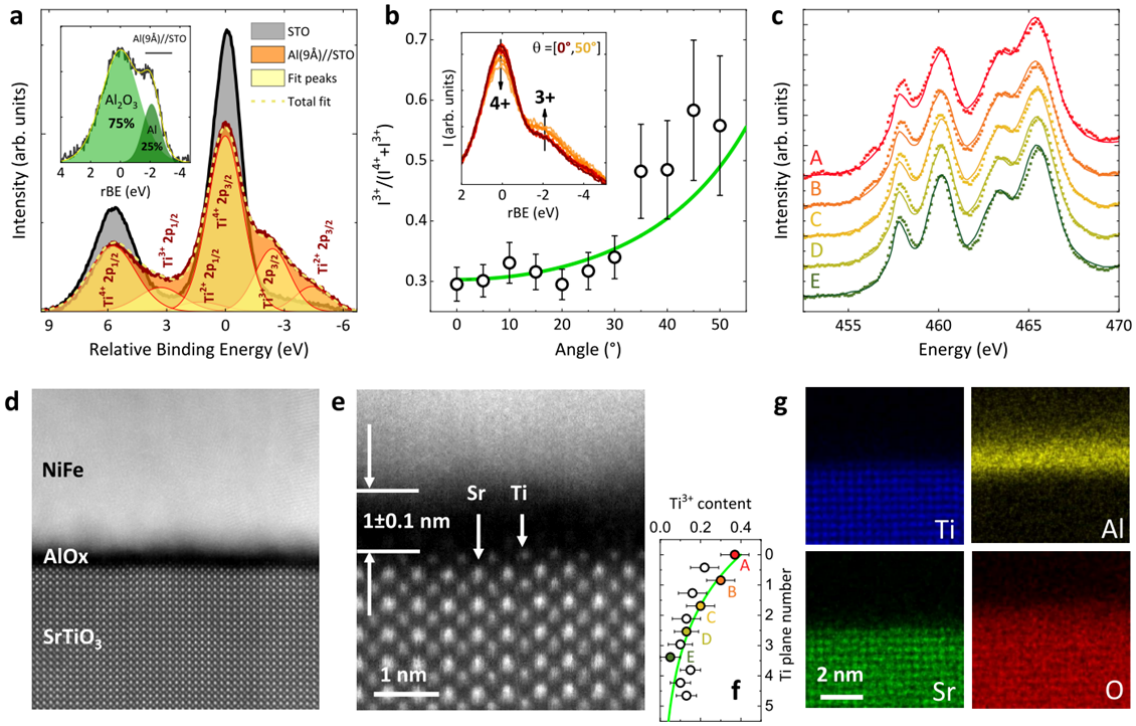

Figure 1. Characterization of AlO_x/STO 2DEGs. *(a). X-ray photoelectron spectra near the Ti 2p state for a STO single crystal before (black) and after (red) deposition of 9 Å of Al. Inset: spectrum at the Al 2p state after deposition of 9 Å of Al on STO; rBE stands for relative binding energy. (b) Ti^{3+} fraction for different take-off angles. The error bars come from the fitting process using CasaXPS (see Methods). The experimental spectra are shown in the inset. The green line is a fit using the model of Ref. [19]. (c) EELS spectra at positions indicated in (f) in $SrTiO_3$ (dotted) with simulations (lines) using linear combinations of Ti^{3+} and Ti^{4+} spectra corrected for instrumental resolution. (d) Scanning transmission electron microscopy image. (e) Magnified view of (d). (f) Variation of the Ti^{3+} content deduced from simulations shown in (c) as a function of position in $SrTiO_3$. The green line is an exponential fit. (g) EDX maps.*

We now turn to the transport properties. The temperature dependence of the sheet resistance for a AlO_x/NiFe/AlO_x/STO sample and a AlO_x/NiFe/STO reference sample is displayed in Fig. 2a. Without the Al insertion (brown curve), the resistance shows practically no change over the whole range of temperatures. In contrast, in the full stack (black curve) a drop in resistance is observed below 100 K, signalling an additional conduction path corresponding to the 2DEG. The red curve represents the isolated 2DEG contribution, deduced through a two-channel parallel conduction model[16]. Hall traces of the 2DEG were extracted[16] from Hall measurements at T = 7 K while applying a back-gate voltage V_g. While a non-linear Hall signal was obtained for large positive gate voltages, decreasing V_g promoted a more linear dependence, suggesting that a transition between multi-band and single-band transport occurs. Fitting the Hall traces in the linear regime and using capacitance measurements[20] we obtained the mobile carrier densities in both regimes. As visible in Fig. 2b, the carrier density varies from about 7×10^{13} cm^{-2} at -175 V to 1×10^{14} cm^{-2} at +175 V. We note that, as often reported in STO 2DEGs, the density of mobile carriers is significantly lower than the total electron concentration inferred from core level spectroscopy[19], suggesting the existence of a large fraction of localized electrons.

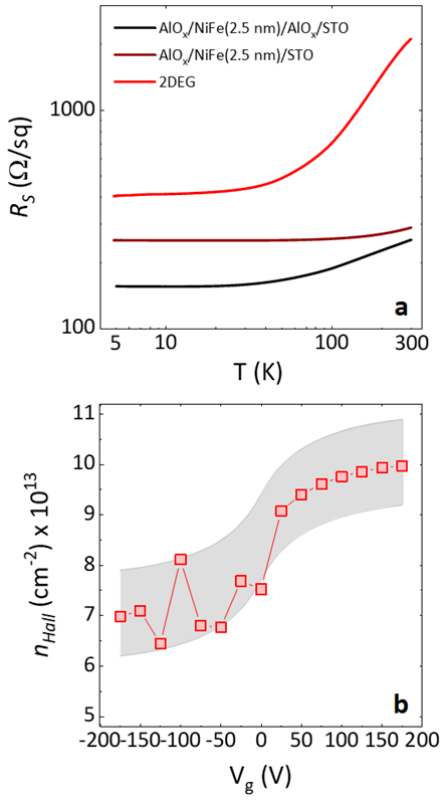

Figure 2. Magnetotransport properties. *(a) Temperature dependence of the sheet resistance of a AlO_x/NiFe/AlO_x/STO sample (black) and a AlO_x/NiFe/STO reference sample, with a deposited Al*

thickness of 9 Å (brown). The extracted contribution from the 2DEG is shown in red. (b) Carrier density as a function of gate voltage. The shaded area, derived from the capacitance measurement, corresponds to the uncertainty in the determination of n_{Hall}.

To characterize the IEE in our AlO_x/STO 2DEGs, we used spin pumping ferromagnetic resonance (FMR) experiments at 15 K on a AlO_x/NiFe(20 nm)/AlO_x/STO sample with a nominal deposited Al thickness of 9 Å (see Methods). Fig. 3a depicts the principle of the technique: DC and radio frequency (rf) magnetic fields H_{DC} and h_{rf} are applied to excite magnetization precession in the NiFe layer. At ferromagnetic resonance, a pure spin current is injected in the 2DEG[21]. In the presence of IEE, a transverse DC voltage will be generated. Fig. 3b shows FMR signals (top panels) at different gate voltages. The FMR resonance field and the linewidth do not vary, implying that the gate voltage does not affect the properties of the ferromagnet. The bottom panels of Fig. 3b show the voltage signals produced at resonance, possessing two components: a symmetric one and a much smaller antisymmetric one (V_{sym} and V_{asym}, *respectively*), both of which are reversed upon reversing H_{DC}. While the antisymmetric component arises from spin rectification effects such as anisotropic magnetoresistance, the symmetric component (spin signal) is due to spin-charge conversion (by inverse spin Hall effect – ISHE – or IEE). For all gate voltages shown, V_{sym} strongly dominates the signal, pointing to a high spin-charge conversion efficiency. In addition, the signal was observed to be linear with the rf power, for a maximum of 5 mW.

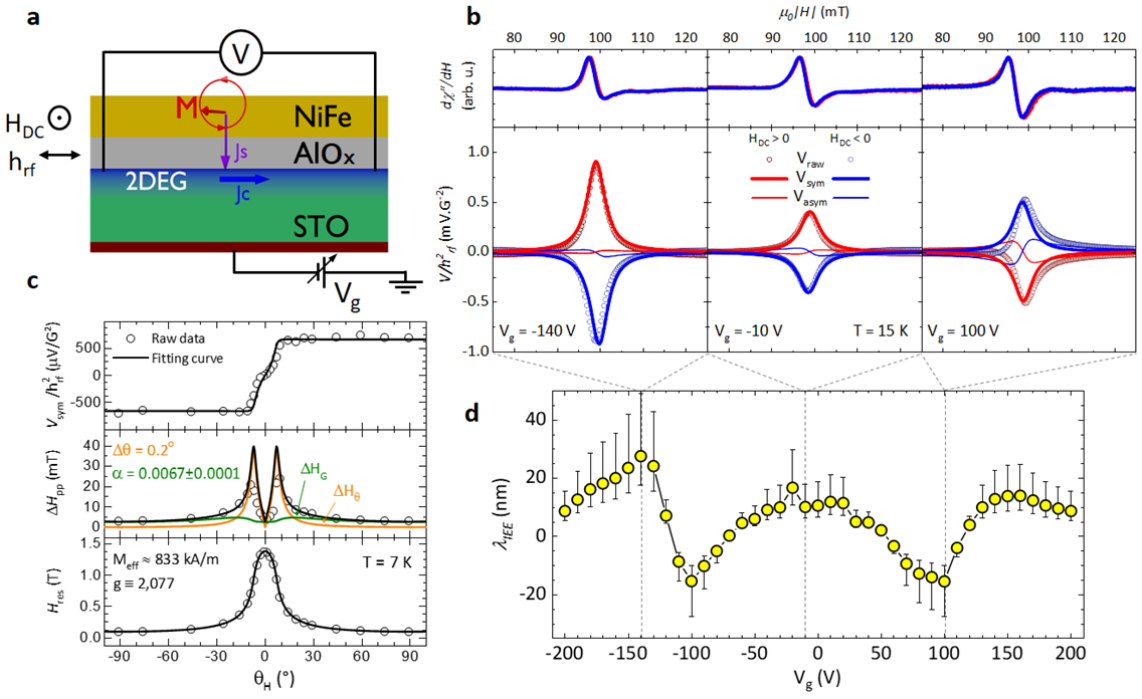

Figure 3. Spin-charge conversion in NiFe/AlO_x/STO. *(a) Sketch of the spin pumping experiment. (b) FMR curves (top) and spin signals (bottom) for different values of the gate voltage, for a positive (red)*

and negative (blue) applied DC magnetic field. The symmetric V_{sym} and antisymmetric V_{asym} components of the raw spin signals V_{raw} are represented using continuous thick and thin lines, respectively. (c) Top panel: angular out-of-plane dependence of the amplitude of the symmetric component of the spin-pumping signal, normalized by the square of the applied rf field. Center panel: angular out-of-plane dependence of the ferromagnetic resonance peak-to-peak linewidth. The fit enables the separation of the contributions of the damping (ΔH_G) and the magnetic inhomogeneities in the FM layer (ΔH_0), thus allowing the extraction of the damping parameter α. Bottom panel: angular out-of-plane dependence of the ferromagnetic resonance field. The fit allows the extraction of the magnetization and g-factor. All the fits have been made using the model proposed in Ref.[22] *(d) Spin-charge conversion efficiency λ_{IEE} as a function of gate voltage at 15 K. The error bars come from the uncertainty in the determination of the spin mixing conductance (see Supplementary Material).*

The out-of-plane angular dependence of the spin signal amplitude, shown in Fig. 3c, is in agreement with the theoretical expectations for ISHE or IEE[22]. The out-of-plane angular dependences of the ferromagnetic resonance peak-to-peak linewidth ΔH_{pp} and the ferromagnetic resonance field H_{res} allow the extraction of the magnetization M_{eff}=833 kA.m^{-1}, the g-factor g=2.077 and the damping α=0.0066 that are typical of a 20 nm thick NiFe film.

The value of j_S^{3D} can then be calculated by comparing the value of α with that of a reference NiFe/Si sample[21]; the spin mixing conductance was $G_{eff}^{\uparrow\downarrow}$=2.2±1 nm^{-2} (see Supplementary Material). j_C^{2D} can be extracted from the spin signal value and the sample resistivity[4]. From j_S^{3D} and j_C^{2D} we calculate λ_{IEE} and plot its gate dependence in Fig. 3d. The spin-charge conversion varies strongly in sign and amplitude, with its sign changing several times in the studied range of gate voltages. Moreover, the conversion efficiencies at maximum values are extremely high, for both positive and negative values (+28 nm, -16 nm). These efficiencies are, in absolute value, much higher than those measured in other spin-orbit systems. In spin Hall materials, λ_{IEE} can be compared to the product of the spin Hall angle and the spin diffusion length, and typical values are below 1 nm for Pt or W[23]. In topological insulators, λ_{IEE} values go up to 2.1 nm in α-Sn (Ref. [5]), 2.0 nm in HgTe (Ref. [24]), and 0.08 nm in (Bi, Sb)Te (Ref. [25]). The conversion efficiency observed here is also higher than what can be obtained in Rashba interfaces (0.3 nm in Ag/Bi, Ref. [4]), or even in previously studied oxide-based systems (6.4 nm in LAO/STO, Ref. [10], and 0.6 nm in Cu/Bi_2O_3, Ref. [26]).

To gain more insight into the relationship between the IEE effect and the electronic structure of STO 2DEGs, we have performed angle-resolved photoemission experiments on Al/STO and vacuum-cleaved STO samples with integrated carrier densities in the 10^{13}-10^{14} cm^{-2} range (see Supplementary Material). Fig. 4a displays the ARPES Fermi surface of a 2DEG stabilized at the (001) surface of STO for

a sample with $n \approx 1.5 \times 10^{14}$ cm^{-2}. In bulk STO, d_{xy}, d_{yz}, and d_{zx} bands near the Fermi energy are hybridized due to spin-orbit interaction. The confinement in the 2DEG leads to the creation of sub-bands and the emergence of an unconventional Rashba effect with a spin splitting that is enhanced in certain k-space areas[27–29] due to orbital mixing. We resolve three concentric circular contours centred at the Γ_{11} point and two ellipsoidal Fermi surface sheets with major axes along the k_x and k_y direction, respectively, giving four inequivalent bands in total (two heavy and two light bands), consistent with previous studies[17,27,30]. The ellipsoidal features have lower intensity due to the light polarization chosen for this experiment[27]. Electronic structure dispersion plots along the high symmetry directions Γ-X [100] and Γ-M [110] are displayed in Figures 4b and 4c respectively. In the dispersion plot along Δ, shown in Figure 4d, we resolve the lowest lying sub-band that forms the outer Fermi surface sheet. In addition, we observe additional spectral weight at k_Δ=0 located ~15 meV below the Fermi level (see Supplementary Material).

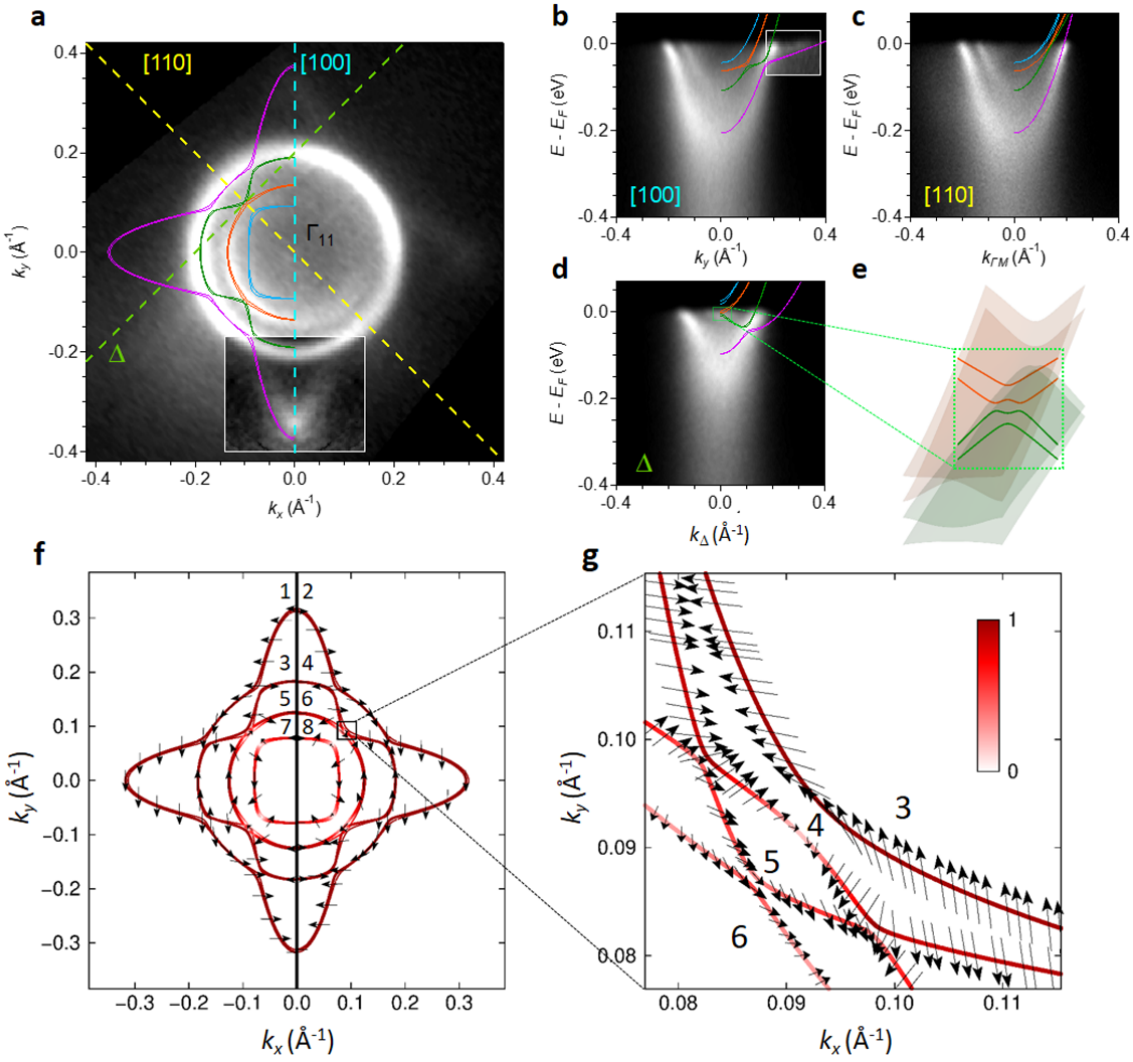

Figure 4. Electronic and spin structure of the 2DEG. *(a) Experimental Fermi surface of the 2DEG around the Γ_{11} point. (b) Band dispersion along the [100] direction – cf. cyan dashed line in (a), with overlaid bands calculated by an eight-band tight-bonding model. (c) Same along the [110] direction – cf. yellow dashed line in (a). The insets to (a,b) use an enhanced contrast to better visualize the faint heavy bands (see Methods). (d) Same along the Δ direction – cf. green dashed line in (a). (e) Calculated band structure along Δ near k_c. (f) Calculated Fermi surface and spin expectation values (direction: arrows, absolute value: color scale) at an energy near the band inversion region, where the left (right) panel corresponds to the outer (inner) band of each pair. The numbers denote the band in energetically ascending order. (g) is a zoom-in near k_c (boxed region in f).*

Next, we derive a model Hamiltonian that reproduces the ARPES measurements. We take into account the two energetically lowest d_{xy} bands and one d_{yz} and d_{zx} band, respectively. Accounting for spin, this results in an eight-band effective Hamiltonian (see Methods), which reproduces the measured ARPES band structure very well (Fig. 4a-d). Fig. 4e shows the calculated band structure along a Δ direction (perpendicular to the [110] direction). Because of the interplay between spin-orbit coupling and orbital mixing, the band structure shows a band inversion with an avoided crossing at the critical k point k_c (corresponding to k_Δ=0). This band inversion renders the 2DEG topologically non-trivial and gives rise to spin-polarized topological edge states that have been predicted in Ref.[31] by means of the Z_2 topological invariant. Figs. 4f and 4g show the spin expectation value for all eight bands. The band inversion discussed in Fig. 4d and 4e leads to strong modulations of the spin expectation values near the Fermi energy. Indeed, as observed in Fig. 4g, the spin expectation value almost vanishes in the fourth band near k_c, while it remains considerable in the third band, leading to uncompensated spin textures.

Let us now examine how this peculiar band structure produces spin-charge interconversion. We characterize the direct Edelstein effect efficiency by the tensor $\hat{\boldsymbol{\kappa}}$ that relates the spin $\boldsymbol{s}$ per surface unit cell to the externally applied electric field $\boldsymbol{E}$, $\boldsymbol{s} = \hat{\boldsymbol{\kappa}}\boldsymbol{E}$. In Fig. 5b, we plot the direct Edelstein efficiency κ_{xy} calculated from the spin expectation values for different Fermi energies (assuming a rigid band shift) using a semi-classical Boltzmann approach (see Methods). Since the EE is the Onsager reciprocal of the inverse Edelstein effect[9] (in the approximation of transparent interfaces), the experimental data of Fig. 3d (that we replot in Fig. 5a) can be compared with the theoretical results. At low energy, only the two low-lying d_{xy} sub-bands (❶ in Fig. 5c) are occupied and κ_{xy} is relatively small, consistent with the modest Rashba-like splitting of these bands. Upon increasing energy, a step occurs corresponding to the population of the next d_{xy} sub-band pair (❷) followed by an extremum signaling the onset of the first heavy sub-band pair (❸). Then, κ_{xy} decreases and

changes sign, owing to the alternating sign of the spin splitting between the d_{xy} and the first pair of $d_{zx,yz}$ bands[29,32] (as discussed in Ref.[11]), reaching a large negative value corresponding to the trivial avoided crossing (❹), i.e. the first crossing between light d_{xy} and heavy $d_{zx,yz}$ bands where orbital mixing enhances Rashba splitting[27]. Another extremum followed by a slope change of κ_{xy} occurs at the band edge of the second pair of $d_{zx,yz}$ bands, again due to opposite spin splitting compared to the fifth and sixth bands (❺), as seen in the light blue curve of Fig. 5b (top panel). Upon further increasing energy, the topological band inversion is reached (❻) where the uncompensated spin texture between the third and fourth bands causes a pronounced maximum in the Edelstein signal. This large spin-charge conversion efficiency is a consequence of the *topological order* in the system. We point out, however, that it is not caused by topological edge states themselves, whose contributions would compensate at opposite edges of the 2DEG.

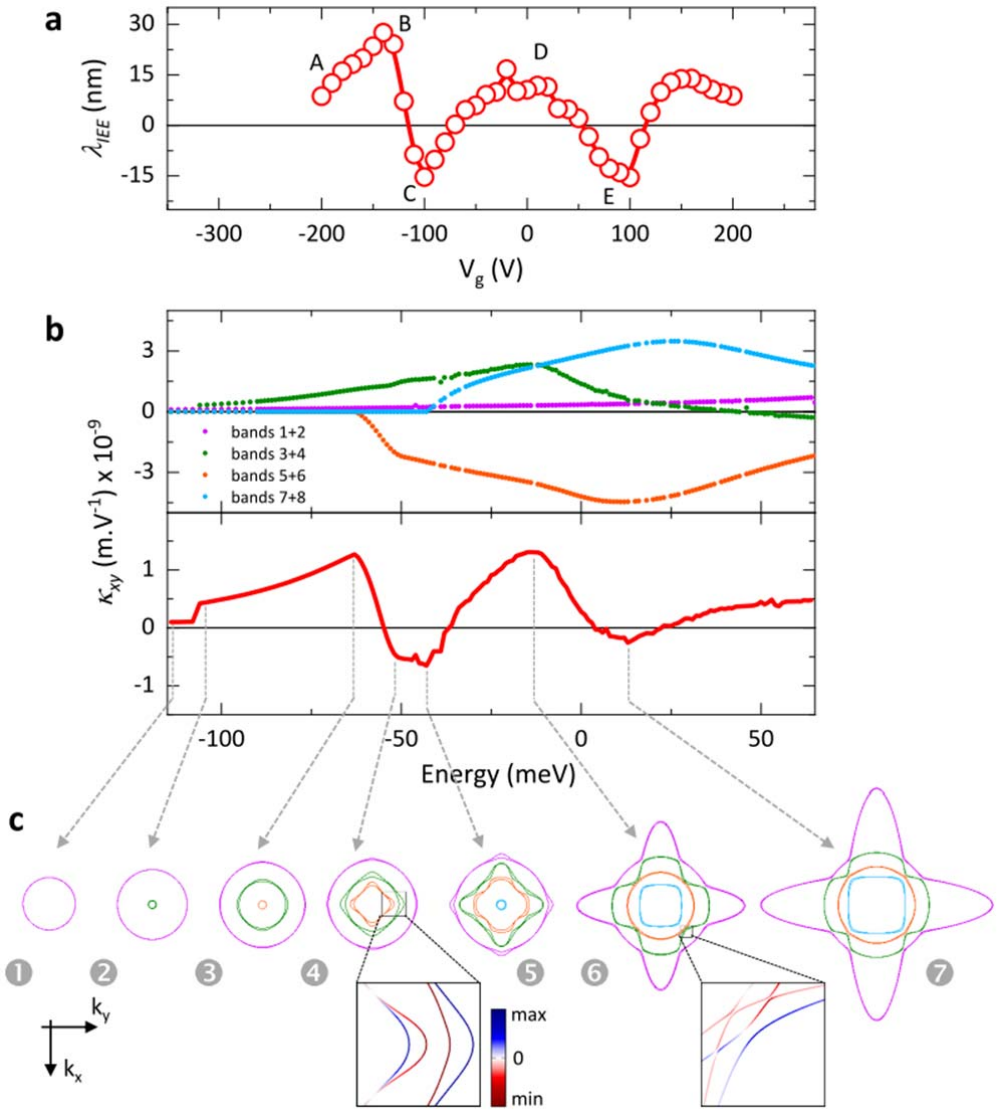

Figure 5. Energy dependence of the spin-charge conversion. *(a) Gate dependence of λ_{IEE} at 15 K. (b) Energy dependence of the Edelstein tensor (top: band-resolved; bottom: total). (c) Fermi lines at various energies. ❶ Rashba-like bands 1+2. ❷ Edge of bands 3+4. ❸ Edge of bands 5+6. ❹ Trivial avoided crossing. ❺ Edge of bands 7+8. ❻ Topologically non-trivial avoided crossing (with band inversion). ❼ Maximum from multiple bands. The colour scale of the zoom-in regions in ❹ and ❻ corresponds to the contribution of each state to the Edelstein effect.*

While the trivial avoided crossing in the [100] direction (❹) unlocks only an enhanced Rashba spin splitting due to orbital mixing, the topologically non-trivial avoided crossing in the Δ direction adds a large contribution from the uncompensated spin texture (see both insets of Fig. 5c), which drives the overall Edelstein effect to large values in this region. This can be better understood by recalling the nature of the Edelstein effect in a Rashba system, where the net spin-charge current produced arises from the inequivalence of the Fermi contours. If the spin splitting between bands is larger, i.e. if Fermi contours have very different sizes, this inequivalence is enhanced. A similar result is intuitively obtained if the spin-split bands have uncompensated spin textures, where the spin current produced through the EE by one contour would be much larger than the one produced by its Rashba-split counterpart. Lastly, for even higher energy, another sign change occurs followed by a negative extremum, resulting from the competing contributions from multiple bands (❼).

Remarkably, the calculated κ_{xy} curve qualitatively reproduces the occurrence of extrema and sign changes in the IEE signal. However, the presented energy range cannot be unambiguously related to the depicted gate voltage. To gain more insight into their correspondence, we have performed Poisson-Schrödinger calculations of the energy spectrum for an STO interface (see Supplementary Material). They indicate that to shift the Fermi level from the expected energy of the topologically avoided crossing to the trivial avoided crossing, the 2DEG needs to be depleted by Δn=2.6×10^{13} cm^{-2}. By matching these two points in Fig. 5c (❻ and ❹) with points D and C in Fig. 5a, we observe that V_G was swept between about 0-20 V and -100 V, respectively. According to the transport data in Fig. 2b, this range of gate voltages is equivalent to a depletion of Δn=1.7±1×10^{13} cm^{-2}, compatible with the estimation from Poisson-Schrödinger calculations.

Although the energy dependence of λ_{IEE} and κ_{xy} are quite comparable and can be related to the spin splittings of the band structure of the AlO_x/STO 2DEG, the explanation of the extremely large IEE signal needs another ingredient. In the theoretical description scattering is restricted to the 2DEG only. In the experiments, however, the electrons have in principle the possibility to leak out of the 2DEG through a tunneling barrier (in this case, the AlO_x layer), and scatter in the metal with very short relaxation times (typically tens of fs). This can be considered as a second scattering channel[33,34]

characterized by an escape time τ_{esc} through the tunneling barrier, in addition to the scattering between the STO states with characteristic time τ_{2DEG}. The two scattering channels lead to an effective relaxation time $\tau_{eff}=(\tau_{2DEG}^{-1} + \tau_{esc}^{-1})^{-1}$ that will set the efficiency of the conversion process. The strength of this second scattering channel can modify the IEE signal considerably. Long escape times would change the IEE signal only slightly and result in an optimal spin-charge conversion signal, while short escape times, as in metallic interfaces such as Ag/Bi[4], would considerably reduce τ_{eff} and consequently the IEE signal. We can use this picture to compare the values of λ_{IEE} found in NiFe/LAO//STO samples[10] and here in NiFe/AlO_x//STO. We deduce the escape times through 2 uc LAO and ~1 nm of AlO_x from their estimated resistance area (RA) product (through $\tau_{esc} = \frac{RAe^2m^*}{2\pi\hbar^2}$ with RA≈10 Ω.µm² and 10^5 Ω.µm², respectively). This leads to escape times in the ps range for 2 uc of LAO and in the 10 ns range for 1 nm of AlO_x. We see that for 2 uc of LAO τ_{esc} is comparable to or shorter than the momentum relaxation of the 2DEG τ_{2DEG}, estimated to 1-10 ps, which should lead to a reduction of λ_{IEE} compared to an isolated 2DEG. On the other hand, for the present NiFe/AlO_x/STO samples, τ_{esc} is much longer than τ_{2DEG}: the electrons will scatter within the 2DEG before having a chance to leak out to the metal. In this case, the 2DEG is well isolated from the metal by the alumina barrier, and λ_{IEE} can approach its optimum value.

Finally, to evaluate the application potential of our system, we have performed spin pumping experiments to determine the expected output voltage at room temperature. This quantity, given by the product of λ_{IEE} and the sheet resistance, is the figure of merit for devices and is relevant for instance for the spin transistor proposed by Intel (MESO device)[36]. Since λ_{IEE} is proportional to the momentum relaxation time (and thus to the electron mobility) one expects a strong decrease of λ_{IEE} upon increasing the temperature, but in parallel the sheet resistivity should increase correspondingly and largely compensate this decrease. For the present heterostructure we find a considerable λ_{IEE}=0.5±0.1 nm at room temperature, and a sheet resistance on the order of 2.5 kΩ. The output voltage in the MESO device can be calculated from

$$V_{out} = P\lambda_{IEE}J_{supply}wR_S$$

with P the spin polarization, J_{supply} the supply current density and w the device width. Taking $P = 0.5$, $J_{supply} = 5\times10^{10}$ A/m² and $w =$ 300 nm, we obtain $V_{out} \approx$ 10 mV, just one order of magnitude lower than the targeted value of 100 mV. This has to be compared with the value of V_{out} one can estimate for a Pt film of 5 nm in thickness (t), that would have $R_S = \rho/t$ =20 Ω and an equivalent $\lambda_{IEE} = \theta_{SHE}l_{sf}$ with $\theta_{SHE} = 0.06$ the (inverse) spin Hall angle and $l_{sf} = 4$ nm the spin diffusion length, leading to $\lambda_{IEE} = 0.2$ nm. This yields $V_{out} = 0.03$ mV, i.e. two to three orders of magnitude less than with our STO 2DEG.

In summary, we have reported spin-charge conversion in an oxide 2DEG formed by the room-temperature sputtering deposition of Al on $SrTiO_3$, with an efficiency about two orders of magnitude larger than that of the canonical spin-orbit coupling material, Pt. We have related the amplitude of the effect and its strong gate dependence to the band structure of the 2DEG, possessing trivial and topological avoided crossings, and to the high tunnel resistance of the Al oxide layer. Highly-doped STO-based oxide interfaces thus emerge as new members of the family of topological two-dimensional materials, able to realize specific functions for spintronics devices. Our observation of a finite spin-charge conversion effect at room temperature, combined with the high resistance of the 2DEG and the scalable room-temperature preparation process qualifies STO interfaces as very promising materials for non-volatile spin logic architectures[36,37]. More fundamentally, our results should stimulate the search for topological phenomena in other oxide 2DEGs[38] and interfaces based on elements heavier than Ti that could produce even stronger spin-charge interconversion effects and possibly harbour more exotic states of matter[39].

ACKNOWLEDGMENTS

This work received support from the ERC Consolidator Grant #615759 ''MINT'', the QUANTERA project "QUANTOX", the French ANR programme through projects OISO (ANR-17-CE24-0026-03), TOPRISE (ANR-16-CE24-0017) and the Laboratoire d'Excellence LANEF (ANR-10-LEBX-51-01). MB thanks the Alexander von Humboldt Foundation for supporting his stays at Martin-Luther-Universität Halle. FT acknowledges support by research grant VKR023371 (SPINOX) from VILLUM FONDEN. AJ, BG and IM acknowledge support by Priority Program SPP 1666 and SFB 762 of Deutsche Forschungsgemeinschaft (DFG). DCV thanks the French Ministry of Higher Education and Research and CNRS for financing his PhD thesis. We thank H. Jaffrès for insightful comments on tunnel escape times, M. Sing for his help with XPS analysis and E. Schierle for his assistance with X-ray absorption spectroscopy measurements.

AUTHOR CONTRIBUTIONS

MB proposed and supervised the study with help from LV, J-PA, AB and AF. DCV prepared the samples with the help of FT and LMVA and performed XPS experiments and analysed the data with AS. DCV, GS and NB measured the magnetotransport properties and analysed the results. HO prepared the samples for STEM and EELS and performed the observations and spectroscopy measurements. SV performed the X-ray absorption measurements and analysed the data. SMW, FYB

and FB performed the ARPES measurements and their analysis. PN performed the spin-pumping experiments and analysed the data with DCV, LV, J-PA and MB. PB, MV and MG conducted the Poisson-Schrödinger calculations. AJ and BG performed the tight-binding and Boltzmann calculations under the supervision of IM, with inputs from MV, MG and MB. DCV and MB wrote the manuscript with inputs from all authors. All authors discussed the results and contributed to their interpretation.

DATA AND CODE AVAILABILITY STATEMENT

The data that support the findings of this study are available from the corresponding author upon reasonable request. The self-written code that generated the data for Figs. 4f,g and 5b,c is available from AJ upon reasonable request.

METHODS

Sample preparation. NiFe and Al films were deposited at room temperature by dc magnetron sputtering on TiO_2-terminated (001)-oriented STO substrates (from CrysTec GmbH). TiO_2-termination was achieved through a chemical treatment, where the substrate was submerged in a buffered hydrofluoric acid (NH_4F-HF 7:1) for 30 s and annealed under a rich oxygen environment at 1000 °C for 3 h. Prior to in situ XPS or sputtering procedures, the STO substrate was additionally annealed at 730 °C for 2 h under a partial oxygen pressure of 400 mbar. The deposition of the metallic layers was performed under an Ar partial pressure of 4.5 x 10^{-4} mbar and a substrate-to-target distance of 7 cm. The deposition rates of the Al ultra-thin layer (0.9 nm) and the NiFe layers (2.5 nm for transport and 20 nm for spin pumping experiments) was 0.1 and 0.2 nm/s, under an operating dc current of 30 and 80 mA, respectively. Samples used for transport and spin pumping were additionally capped with a 2.5 nm layer of Al, which becomes oxidized when exposed to air.

X-ray photoemission spectroscopy was performed using a non-monochromatized Mg Kα source (h_v = 1253.6 eV) on 10 mm x 10 mm STO and Al(0.9nm)/STO samples. Spectra analysis was carried out with the CasaXPS software. From a previous work[16], the maximum probing depth for this system is estimated to be ~5 nm. The error bars displayed in the angle dependence experiments were calculated through the error propagation of $Ti^{3+}/(Ti^{4+}+Ti^{3+})$ spectral areas, obtained individually from Monte Carlo simulations in CasaXPS.

Scanning transmission electron microscopy measurements have been carried out using a Cs-corrected FEI Themis at 200 keV. HAADF-STEM images were acquired using a convergence semiangle of 20 mrad and collecting scattering from >65 mrad. Energy dispersive X-ray spectroscopy (EDX) was performed for elemental mapping using a Brucker EDX system consisting of four silicon drift detectors in the Themis microscope. STEM specimens were prepared by the FIB lift-out technique using a FEI dual-beam Strata 400S at 30 kV. EELS measurements were performed at 80 kV using a double-aberration-corrected FEI Titan Ultimate TEM equipped with a high brightness electron source and a Gatan Quantum energy filter equipped with Dual EELS. The probe corrector was used to obtain a beam current of 120 pA while maintaining nanometer resolution. The core loss region was recorded over the range 400–600 eV at a dispersion of 0.1 eV $pixel^{-1}$.

Magnetotransport measurements were performed with a PPMS system from Quantum Design after bonding the samples with Al wires. The electrical contribution coming only from the 2DEG was isolated using the method discussed in Ref.[16]. The variation of the carrier density n_{2D} is obtained by integrating the gate capacitance $C_g(V_g)$ measured by a standard lock-in technique, over the gate voltage range: $n_{2D} = n_{2D}(V_g < 0\ V) + \frac{1}{eA}\int_{-175\ V}^{V_g} C_g(V)\, dV$ where A is the area of the sample and

$n_{2D}(V_g < 0\,V)$ is matched to the maximum and minimum Hall carrier densities experimentally obtained in the underdoped regime.

Spin Pumping. The spin-pumping experiments were carried out using a Bruker ESP300E X-band CW spectrometer at 9.68 GHz, with a loop-gap Bruker ER 4118X-MS5 cavity, and using a microwave power of 5 mW or less to remain in the linear regime. The generated DC voltage was measured using a Keithley 2182A nanovoltmeter. The gate voltage was applied using a Keithley 2400 sourcemeter. The sample was initialized by sweeping the back-gate voltage from +200 V to −200 V, and then back to +200 V, to avoid any hysteretic behavior. The measurement was then performed for different gate voltages, from +200V to -200V.

Angle-resolved photoemission. ARPES measurements were performed at the SIS beamline of the Swiss Light Source. A single crystal of $SrTiO_3$ slightly doped with La (0.075 wt%) was used to perform the experiments. The introduction of La as a dopant results in a small residual bulk conductivity that helps to avoid sample charging during the experiment. The crystal was cleaved in situ at the measurement temperature of T = 15 K in a pressure lower than 10^{-10} mbar. The surface was exposed to synchrotron light of 51 eV in order to saturate the bandwidth of the 2DEG[30]. After this procedure ARPES measurements were taken using linear horizontal polarized photons with an energy of 51 eV. The combined energy resolution was ~20 meV. In the insets of Fig. 4 (a,b) we have enhanced the contrast by dividing the data by a smooth function of momentum. We verified that this procedure does not significantly change the position of peaks.

Tight-binding model. The Hamiltonian is a generalized version of that from Ref.[31] We consider the two energetically lowest d_{xy} bands and one d_{yz} and d_{zx} band, respectively. The Hamiltonian includes spin, nearest-neighbor hopping (quantified by t, t_h), spin-orbit interaction (λ) and orbital mixing (g_1, g_2)

$$H = \begin{pmatrix} \epsilon_{xy1} & 0 & f_{1x} & f_{1y} & 0 & 0 & \lambda & -\mathrm{i}\lambda \\ 0 & \epsilon_{xy2} & f_{2x} & f_{2y} & 0 & 0 & \lambda & -\mathrm{i}\lambda \\ -f_{1x} & -f_{2x} & \epsilon_{yz} & \mathrm{i}\lambda & -\lambda & -\lambda & 0 & 0 \\ -f_{1y} & -f_{2y} & -\mathrm{i}\lambda & \epsilon_{zx} & \mathrm{i}\lambda & \mathrm{i}\lambda & 0 & 0 \\ 0 & 0 & -\lambda & -\mathrm{i}\lambda & \epsilon_{xy1} & 0 & f_{1x} & f_{1y} \\ 0 & 0 & -\lambda & -\mathrm{i}\lambda & 0 & \epsilon_{xy2} & f_{2x} & f_{2y} \\ \lambda & \lambda & 0 & 0 & -f_{1x} & -f_{2x} & \epsilon_{yz} & -\mathrm{i}\lambda \\ \mathrm{i}\lambda & \mathrm{i}\lambda & 0 & 0 & -f_{1y} & -f_{2y} & \mathrm{i}\lambda & \epsilon_{zx} \end{pmatrix},$$

with the diagonal elements

$$\epsilon_{xyj} = 2t\left[2 - \cos(k_x) - \cos(k_y)\right] + o_j,$$
$$\epsilon_{yz} = 2t\left[1 - \cos(k_y)\right] + 2t_h[1 - \cos(k_x)] + o_3,$$

$$\epsilon_{zx} = 2t\,[1-\cos(k_x)] + 2t_h\big[1-\cos\big(k_y\big)\big] + o_3,$$

418 and the orbital mixing term

$$f_{jm} = 2\mathrm{i}g_j\sin(k_m).$$

419 The parameters are:

$$t = 0.388\ \text{eV}, t_h = 0.031\ \text{eV},$$
$$o_1 = -0.205\ \text{eV}, o_2 = -0.105\ \text{eV}, o_3 = -0.0544\ \text{eV},$$
$$g_1 = 0.002\ \text{eV}, g_2 = 0.005\ \text{eV},$$
$$\lambda = \frac{1}{120}\,\text{eV},$$

420 resulting in a good agreement with the ARPES data (Fig. 4a-d).

421 **Calculation of the Edelstein effect.** The tensor for the Edelstein effect $\hat{\boldsymbol{\kappa}}$ characterizes the spin
422 density per unit cell $\boldsymbol{s}$ as a response to an externally applied electric field $\boldsymbol{E}$

$$\boldsymbol{s} = \hat{\boldsymbol{\kappa}}\boldsymbol{E}.$$

423 It is calculated using the semi-classical Boltzmann transport theory,

$$\kappa_{ij} = \frac{-eA_0}{A}\sum_{\boldsymbol{k}} \langle\sigma\rangle_{\boldsymbol{k}}^{i}\, \Lambda_{\boldsymbol{k}}^{j}\delta(\epsilon_{\boldsymbol{k}} - \epsilon_{\mathrm{F}}).$$

424 Here, A is the area of the system, A_0 is the area of the surface unit cell, $e > 0$ is the elementary
425 charge, and $\langle\boldsymbol{\sigma}\rangle_{\boldsymbol{k}}$ is the spin expectation value of the state at wave vector $\boldsymbol{k}$ and energy $\epsilon_{\boldsymbol{k}}$. The sum
426 is over all k points and all bands. The mean free path $\Lambda_{\boldsymbol{k}} = \tau_0\boldsymbol{v}_{\boldsymbol{k}}$ is approached by the constant
427 relaxation time approximation $\tau_0 = 1$ ps. At zero temperature, only states at the Fermi level ϵ_{F}
428 contribute to the Edelstein effect.

429 For the 2DEG Hamiltonian, symmetry only allows for nonzero tensor elements $\kappa_{xy} = -\kappa_{yx}$. Thus, an
430 external electric field induces an in-plane spin density perpendicular to the field, as in Rashba
431 systems.

432 **Poisson-Schrödinger calculations.** The electronic states of the carriers in the 2DEG were determined
433 with the help of the Poisson-Schrödinger algorithm which self-consistently yields the shape of the
434 electrostatic potential at the interface and the sub-band structure. For a set total electric charge
435 density, we solved the Schrödinger equation for a particle in a potential well, using values of the
436 effective masses corresponding to the hopping parameters t and t_h introduced in the tight-binding
437 model. We also include the atomic spin-orbit coupling in our computation, described by the

parameter λ in the tight-binding Hamiltonian. From the eigenfunctions and eigenenergies of the Schrödinger equation one obtains the density profile and then solving Poisson equation gives the spatial dependence of the electrostatic potential in the material. The procedure is then iterated until self-consistency is achieved.

REFERENCES

1. Bychkov, Y. A. . & Rashba, E. I. Properties of a 2D electron gas with lifted spectral degeneracy. *JETP Lett.* **39,** 78–81 (1984).

2. Manchon, A., Koo, H. C., Nitta, J., Frolov, S. M. & Duine, R. A. New perspectives for Rashba spin–orbit coupling. *Nature Mater.* **14,** 871–882 (2015).

3. Edelstein, V. M. M. Spin polarization of conduction electrons induced by electric current in two-dimensional asymmetric electron systems. *Solid State Commun.* **73,** 233–235 (1990).

4. Rojas-Sánchez, J. C. *et al.* Spin-to-charge conversion using Rashba coupling at the interface between non-magnetic materials. *Nature Commun.* **4,** 2944 (2013).

5. Rojas-Sánchez, J.-C. *et al.* Spin to Charge Conversion at Room Temperature by Spin Pumping into a New Type of Topological Insulator: α-Sn Films. *Phys. Rev. Lett.* **116,** 096602 (2016).

6. Han, W., Otani, Y. & Maekawa, S. Quantum materials for spin and charge conversion. *npj Quantum Mater.* **3,** 27 (2018).

7. Johansson, A., Henk, J. & Mertig, I. Edelstein effect in Weyl semimetals. *Phys. Rev. B* **97,** 085417 (2018).

8. Zhang, S. & Fert, A. Conversion between spin and charge currents with topological insulators. *Phys. Rev. B* **94,** 184423 (2016).

9. Shen, K., Vignale, G. & Raimondi, R. Microscopic Theory of the Inverse Edelstein Effect. *Phys. Rev. Lett.* **112,** 096601 (2014).

10. Lesne, E. *et al.* Highly efficient and tunable spin-to-charge conversion through Rashba coupling at oxide interfaces. *Nature Mater.* **15,** 1261–1266 (2016).

11. Seibold, G., Caprara, S., Grilli, M. & Raimondi, R. Theory of the Spin Galvanic Effect at Oxide Interfaces. *Phys. Rev. Lett.* **119,** 256801 (2017).

12. Ohtomo, A. & Hwang, H. Y. A high-mobility electron gas at the $LaAlO_3/SrTiO_3$ heterointerface. *Nature* **427,** 423–6 (2004).

13. Caviglia, A. D. *et al.* Electric field control of the $LaAlO_3/SrTiO_3$ interface ground state. *Nature* **456,** 624–7 (2008).

14. Thiel, S., Hammerl, G., Schmehl, A., Schneider, C. W. & Mannhart, J. Tunable quasi-two-dimensional electron gases in oxide heterostructures. *Science* **313,** 1942–1945 (2006).

15. Lesne, E. *et al.* Suppression of the critical thickness threshold for conductivity at the $LaAlO_3/SrTiO_3$ interface. *Nature Commun.* **5,** 4291 (2014).

16. Vaz, D. C. *et al.* Tuning Up or Down the Critical Thickness in $LaAlO_3/SrTiO_3$ through In Situ Deposition of Metal Overlayers. *Adv. Mater.* **29,** 1700486 (2017).

17. Rödel, T. C. *et al.* Universal Fabrication of 2D Electron Systems in Functional Oxides. *Adv. Mater.* **28,** 1976–1980 (2016).

18. Posadas, A. B. *et al.* Scavenging of oxygen from $SrTiO_3$ during oxide thin film deposition and the formation of interfacial 2DEG. *J. Appl. Phys.* **105302,** (2017).

19. Sing, M. *et al.* Profiling the Interface Electron Gas of $LaAlO_3/SrTiO_3$ Heterostructures with Hard X-Ray Photoelectron Spectroscopy. *Phys. Rev. Lett.* **102,** 176805 (2009).

20. Hurand, S. *et al.* Field-effect control of superconductivity and Rashba spin-orbit coupling in top-gated $LaAlO_3/SrTiO_3$ devices. *Sci. Rep.* **5,** 12751 (2015).

21. Tserkovnyak, Y., Brataas, A. & Bauer, G. E. W. Enhanced gilbert damping in thin ferromagnetic films. *Phys. Rev. Lett.* **88,** 117601 (2002).

22. Rojas-Sánchez, J.-C. *et al.* Spin pumping and inverse spin Hall effect in germanium. *Phys. Rev. B* **88,** 064403 (2013).

23. Pham, V. T. *et al.* Ferromagnetic/Nonmagnetic Nanostructures for the Electrical Measurement of the Spin Hall Effect. *Nano Lett.* **16,** 6755–6760 (2016).

24. Noel, P. *et al.* Highly Efficient Spin-to-Charge Current Conversion in Strained HgTe Surface States Protected by a HgCdTe Layer. *Phys. Rev. Lett.* **120,** 167201 (2018).

25. Mendes, J. B. S. *et al.* Dirac-surface-state-dominated spin to charge current conversion in the topological insulator $(Bi_{0.22}Sb_{0.78})_2Te_3$ films at room temperature. *Phys. Rev. B* **96,** 180415 (2017).

26. Karube, S., Kondou, K. & Otani, Y. Experimental observation of spin-to-charge current conversion at non-magnetic metal/$Bi2O_3$ interfaces. *Appl. Phys. Express* **9,** 033001 (2016).

27. King, P. D. C. *et al.* Quasiparticle dynamics and spin-orbital texture of the $SrTiO_3$ two-dimensional electron gas. *Nature Commun.* **5,** 3414 (2014).

28. Zhong, Z., Tóth, A. & Held, K. Theory of spin-orbit coupling at $LaAlO_3/SrTiO_3$ interfaces and $SrTiO_3$ surfaces. *Phys. Rev. B* **87,** 161102 (2013).

29. Khalsa, G. & MacDonald, A. H. Theory of the $SrTiO_3$ surface state two-dimensional electron gas. *Phys. Rev. B* **86,** 125121 (2012).

30. McKeown Walker, S. *et al.* Carrier-Density Control of the $SrTiO_3$ (001) Surface 2D Electron Gas studied by ARPES. *Adv. Mater.* **27,** 3894–3899 (2015).

31. Vivek, M., Goerbig, M. O. & Gabay, M. Topological states at the (001) surface of $SrTiO_3$. *Phys. Rev. B* **95,** 165117 (2017).

32. Zhong, Z., Tóth, A. & Held, K. Theory of spin-orbit coupling at $LaAlO_3/SrTiO_3$ interfaces and $SrTiO_3$ *Phys. Rev. B* **87,** 161102 (2013).

33. Kim, J. *et al.* Evaluation of bulk-interface contributions to Edelstein magnetoresistance at metal/oxide interfaces. *Phys. Rev. B* **96,** 140409 (2017).

34. Dey, R., Prasad, N., Register, L. F. & Banerjee, S. K. Conversion of spin current into charge current in a topological insulator: Role of the interface. *Phys. Rev. B* **97,** 174406 (2018).

35. Herranz, G. *et al.* High Mobility in $LaAlO_3/SrTiO_3$ Heterostructures: Origin, Dimensionality, and Perspectives. *Phys. Rev. Lett.* **98,** 216803 (2007).

36. Manipatruni, S. *et al.* Scalable energy-efficient magnetoelectric spin–orbit logic. *Nature* **565,** 35–42 (2019).

37. Manipatruni, S., Nikonov, D. E. & Young, I. A. Beyond CMOS computing with spin and polarization. *Nature Phys.* **14,** 338–343 (2018).

38. Varignon, J., Vila, L., Barthélémy, A. & Bibes, M. A new spin for oxide interfaces. *Nature Phys.* **14,** 322–325 (2018).

39. Xiao, D., Zhu, W., Ran, Y., Nagaosa, N. & Okamoto, S. Interface engineering of quantum Hall effects in digital transition metal oxide heterostructures. *Nature Commun.* **2,** 596 (2011).